



# Stronger Arctic amplification from anthropogenic aerosols than from greenhouse gases



You-Ting Wu<sup>1</sup>, Yu-Chiao Liang<sup>1</sup> ✉, Michael Previdi<sup>2</sup>, Lorenzo M. Polvani<sup>2,3,4</sup>, Mark R. England<sup>5</sup>, Michael Sigmund<sup>6</sup> & Min-Hui Lo<sup>1</sup>

Arctic amplification (AA), the greater Arctic surface warming compared to the global average, has been widely attributed to increasing concentrations of greenhouse gases (GHG). However, less is known about the impacts of other forcings - notably, anthropogenic aerosols (AER) - and how they may compare to the impacts of GHG. Here we analyze sets of climate model simulations, specifically designed to isolate the AER and GHG effects on global climate. Surprisingly, we find stronger AA produced by AER than by GHG during the 1955–1984 period, when the strongest global AER increase. This stronger AER-induced AA is due to a greater sensitivity of Arctic sea ice, and associated changes in ocean-to-atmosphere heat exchange, to AER forcing. Our findings highlight the asymmetric Arctic climate response to GHG and AER forcings, and show that clean air policies which have reduced aerosol emissions may have exacerbated the Arctic warming over the past few decades.

The Arctic climate has undergone dramatic and rapid changes in recent decades<sup>1</sup>. In particular, the Arctic has warmed at a pace faster than the global average, both in observations<sup>2–4</sup>, and in historical simulations from state-of-the-art climate models<sup>3,5–8</sup>. This phenomenon is broadly referred to as Arctic amplification (AA)<sup>4,9,10</sup>. While anthropogenic greenhouse gases (GHG) have been widely recognized as the dominant forcing agent driving AA<sup>9,11,12</sup>, the second largest anthropogenic forcing - anthropogenic aerosols (AER) - may have also played an important role<sup>13–15</sup>. Indeed, previous studies have suggested the possibility of AA associated with increasing aerosol emissions, with stronger cooling in the Arctic than over the rest of the globe<sup>14,16–19</sup>. However, a rigorous examination of this AER-induced AA and its underlying mechanisms, and a quantitative comparison with the effects of GHG, have remain to be carried out.

## Results

To this end, we begin by analyzing the annual mean near-surface air temperature (hereafter SAT) anomalies averaged over the Arctic domain (70°N–90°N) during the 1920–2005 period (Fig. 1a). Three observational estimates of Arctic SAT anomalies (black solid and dashed lines, see Methods) show a gradual warming from 1920 until the 1940s, a subsequent cooling until the late 1970s, and a further warming until the end of the time series in 2005. Global SAT anomalies exhibit a similar temporal evolution,

but with a much smaller magnitude compared to the Arctic SAT anomalies (Fig. 1b, note the scales on the y-axis).

The Arctic and global SAT anomalies derived from the ensemble means of five state-of-the-art climate models (green lines in Fig. 1a, b) with all historical forcings (i.e., GHG, AER, ozone, land-use, and natural forcings, see Methods) resemble the observational SAT anomalies, suggesting that the observed multidecadal SAT variability is largely externally forced as previous studies concluded<sup>10,21</sup>. A question immediately arises: what are the relative roles of GHG and AER, the two most important anthropogenic forcings, in determining the evolution of the Arctic and global SAT anomalies? To answer this question, we analyze the single forcing simulations from the Detection and Attribution Model Intercomparison Project (DAMIP)<sup>22</sup> under the Sixth Phase of the Coupled Model Intercomparison Project (CMIP6)<sup>23</sup>, and the single forcing large ensemble projects from the Community Earth System Model version 1 (CESM1)<sup>24</sup> and an additional set of simulations from the Canadian Earth System Model version 5 (CanESM5)<sup>12,25</sup>. In the DAMIP experiments, climate models are forced only with time-varying GHG or AER, and all other forcings are fixed at pre-industrial levels ("only-one" forcing, see Methods). In contrast, in the CESM1 and in the additional CanESM5 experiments, GHG or AER forcing is held fixed, and all other forcings vary with time ("all-but-one" forcing method, see Methods). In Fig. 1c we show the opposing effects of GHG and AER forcing on the Arctic temperature during

<sup>1</sup>Department of Atmospheric Sciences, National Taiwan University, Taipei, Taiwan. <sup>2</sup>Lamont-Doherty Earth Observatory, Columbia University, Palisades, NY, USA.

<sup>3</sup>Department of Earth and Environmental Sciences, Columbia University, New York, NY, USA. <sup>4</sup>Department of Applied Physics and Applied Mathematics, Columbia University, New York, NY, USA. <sup>5</sup>Department of Mathematics and Statistics, University of Exeter, Exeter, UK. <sup>6</sup>Canadian Centre for Climate Modelling and Analysis, Environment and Climate Change Canada, Victoria, BC, Canada. ✉e-mail: [pamip.yuchiao@gmail.com](mailto:pamip.yuchiao@gmail.com); [yuchiaoliang@ntu.edu.tw](mailto:yuchiaoliang@ntu.edu.tw)

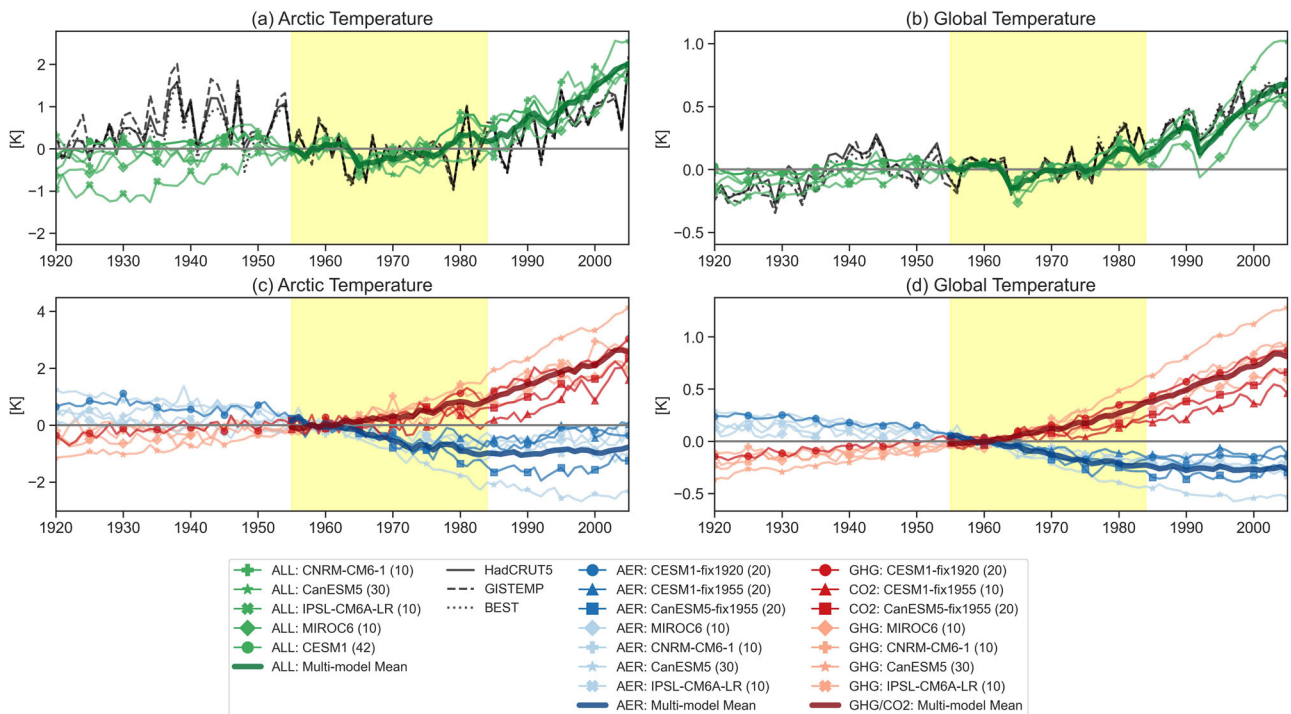
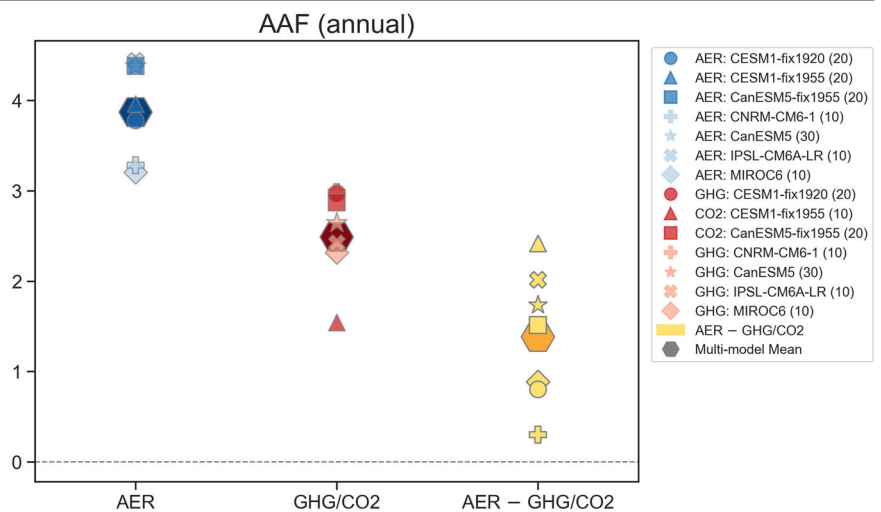


**Fig. 1 | Time evolutions of Arctic and global temperatures from 1920 to 2005.** **a, b** Annual mean Arctic temperature changes and global temperature changes from 1920 to 2005 relative to the mean values from 1955 to 1964, observed (black), and ensemble-mean models under all forcing agents (ALL, green), including CNRM-CM6-1, CanESM5, IPSL-CM6A-LR, MIROC6, and CESM1. **c, d** Annual and

ensemble mean Arctic and global temperature changes under AER forcing (blue) and GHG or CO2 forcing (red). For CO2 effects, we analyzed CESM1-fix1955 and CanESM5-fix1955, while other models are examined under GHG forcing. The yellow shadings represent the 1955–1984 period. The number of ensemble members in each model is denoted in the parenthesis of the figure legend.

**Fig. 2 | Arctic amplification factor (AAF) of AER and GHG.** Annual ensemble mean  $AAF_{AER}$  (blue markers) and  $AAF_{GHG}$  (red markers) for each model, along with the difference between (yellow markers). Large hexagonal markers denote the multi-model-mean values, and the number of ensemble members in each model is indicated in parentheses of the figure legend.



the mid-20<sup>th</sup> century. Here we focus on the 1955–1984 period, the period with the largest global AER increase (Supplementary Fig. 1). Over this period, GHG forcing causes a positive Arctic SAT trend of  $0.35 \pm 0.17\text{K/decade}$  ( $\pm$ denotes the 95% confidence interval hereafter), while AER forcing causes a negative Arctic SAT trend of  $-0.43 \pm 0.22\text{K/decade}$  (red and blue lines in Fig. 1c). After the mid-1980s, the AER-induced cooling halts, owing to the reduction of AER emissions in North America and Europe<sup>26,27</sup>, in contrast to the continued GHG-induced Arctic warming. These patterns are also noticeable in the global average (Fig. 1d), though with reduced magnitudes. The combined effects of GHG and AER largely explain the time-evolving SAT anomalies in response to all forcings (Supplementary Fig. 2).

From an effective radiative forcing (ERF, see Methods) perspective, the fact that GHG- and AER-forced SAT trends during the 1955–1984 are comparable in magnitude is rather surprising, since the trend of AER ERF in the period 1955–1984 ( $-0.18 \pm 0.08 \text{ W/m}^2/\text{decade}$ ) is only about sixty percent of the strength of GHG ERF ( $0.31 \pm 0.07 \text{ W/m}^2/\text{decade}$ ) (Supplementary Fig. 3). This indicates that AER forcing must be more effective in producing Arctic temperature changes than GHG forcing, implying asymmetric Arctic climate responses to AER and GHG forcing agents.

This asymmetric Arctic response is shown in Fig. 2: the AA factor (AAF, see Methods) forced by AER (blue markers, hereafter  $AAF_{AER}$ ) is larger than the one forced by GHG (red markers, hereafter  $AAF_{GHG}$ ) during

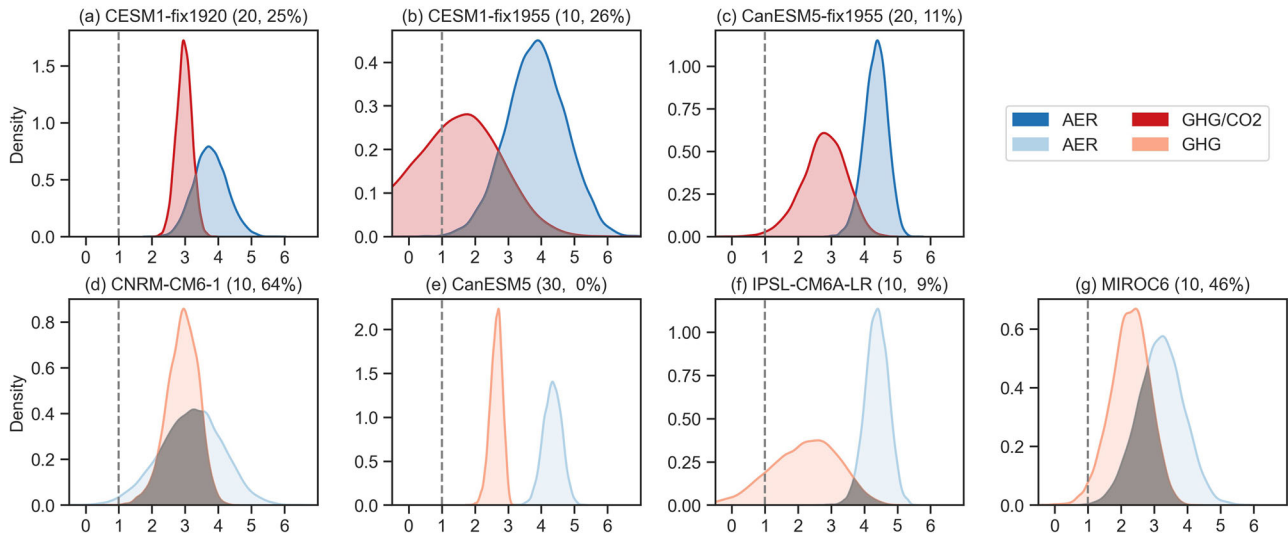


**Fig. 3 | Resampled probability distribution functions (PDFs) to represent the effect of internal variability.** PDFs of  $AAF_{AER}$  (blue) and  $AAF_{GHG}$  (red) for each model (a–g). The overlapping regime between the two curves for each model is

colored in gray, and the two numbers in the title parentheses indicate the number of ensemble members and the overlapping probability (%), respectively.

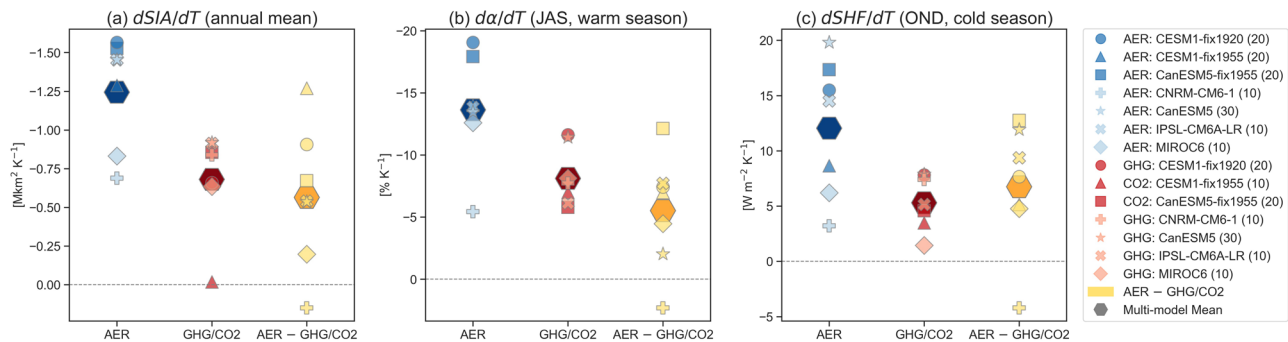


**Fig. 4 | Arctic Sea-ice Area (SIA), albedo, and surface heat flux (SHF) sensitivity to AER and GHG forcings.** a Annual SIA sensitivity under AER (blue markers) and GHG/CO<sub>2</sub> (red markers) for each model, along with the difference between them (yellow markers). b, c The same as a, but for July, August, and September mean (JAS, warm season) albedo sensitivity, and for October, November, and December mean

(OND, cold season) SHF sensitivity. SHF is defined as the sum of net longwave radiation, net shortwave radiation, sensible heat fluxes and latent heat fluxes at the surface. Large hexagonal markers indicate the multi-model mean values, and the number of ensemble members in each model is indicated in parentheses of the figure legend.

the 1955–1984 period. The fact that the difference between  $AAF_{AER}$  and  $AAF_{GHG}$  (yellow markers) is positive for each individual model, and for the multi-model-mean, attests to the robustness of this finding. The differences in AAF across models – for a given forcing – reflect differences in model formulation, the so-called structural uncertainty<sup>28,29</sup>. We quantify this uncertainty by calculating the range of AAF across models, and find similar uncertainties for  $AAF_{AER}$  and  $AAF_{GHG}$  ( $3.87 \pm 0.48$  and  $2.49 \pm 0.51$ , respectively). However, even given this model uncertainty, the means of the two groups of AAFs are statistically distinguishable (c.f., blue and red hexagonal markers in Fig. 2). A recent study has shown that different ways of imposing AER forcing (i.e., the “all-but-one” vs. “only-one” forcing methods) can yield different inferred responses<sup>30</sup>. Three simulation sets used in our study adopt the “all-but-one” forcing method, whereas the other four adopt the “only-one” forcing method. However, we do not find any systematic contrast in AAF between these two groups of models.

In addition to considering differences in model formulation and in the method of imposing a forcing, it is important to recognize the potential role of internal climate variability, which may obscure the forced signal<sup>28,31,32</sup>. To assess and quantify its role, we employ a bootstrapping technique to construct synthetic AAF probability density functions (PDFs, see Methods) across ensemble members of each model (Fig. 3). The width of the PDFs then provides an estimate of the uncertainty in the computed AAFs due to

internal variability, and we also provide the 95% confidence intervals across ensemble members for each model (Supplementary Table S1). It is clear from Fig. 3 that this uncertainty can be large. Owing to the internal variability alone, the AAF can vary by 2 or more from its mean value, resulting in not only some AAFs less than 1 but also overlapping regimes of resampled  $AAF_{AER}$  and  $AAF_{GHG}$  (9–64%, except for 0% in CanESM5). Internal variability noise, thus, hinders a clean separation of the two forced AAFs. Nonetheless, the resampled  $AAF_{AER}$  still contains higher chance to be larger than the resampled  $AAF_{GHG}$  for all models.

To understand the underlying mechanisms leading to larger  $AAF_{AER}$  than  $AAF_{GHG}$ , we examine the Arctic sea-ice response to AER and GHG forcings, and the accompanying changes in atmosphere-ocean heat exchange, which are widely regarded as essential in generating AA<sup>31,33</sup>. We find a greater sea-ice area (SIA) sensitivity to global SAT change in response to AER forcing compared to GHG forcing in most models (Fig. 4a). The only exception to this is CNRM-CM6-1, which is also the model that shows the smallest difference between  $AAF_{AER}$  and  $AAF_{GHG}$  (Figs. 2 and 3d).

Thus far, we have focused solely on the annual-mean response to AER and GHG forcings. However, a complete understanding of Arctic climate change also requires consideration of the seasonality of the response<sup>33–39</sup>. In a warming climate, lower surface albedo (Supplementary Fig. 4a) due to sea-ice retreat allows more absorption of solar radiation by the Arctic Ocean mixed

layer during late summer and early autumn<sup>35,37,39–43</sup>. Subsequently, in late autumn and winter, this excess energy is released to the atmosphere in the form of longwave radiation and latent and sensible heat (Supplementary Fig. 5a), leading to atmospheric warming. The opposite occurs in a cooling climate, with higher surface albedo due to sea-ice expansion, reduced Arctic Ocean absorption of solar radiation in late summer and early autumn, and reduced surface heat flux from the ocean to atmosphere in late autumn and winter (Supplementary Figs. 4b and 5b). When expressed as feedbacks by normalizing by the global SAT change, the surface albedo feedback in summer and surface heat flux feedback in autumn are both found to be stronger in response to AER forcing than GHG forcing in most models, with CNRM-CM6-1 again being the only exception (Fig. 4b, c). These stronger feedbacks with AER forcing help to explain why  $AAF_{AER}$  is larger than  $AAF_{GHG}$ .

## Discussion

To conclude, we find stronger AA from anthropogenic aerosols than that from greenhouse gases during the 1955–1984 period, which is somewhat surprising as the AER radiative forcing is weaker than the GHG one. This is a robust result, which stands out from internal variability, and is not dependent on the choice of climate model or the method used to infer the forced response (i.e., the “all-but-one” or “only-one” forcing method). Stronger sea ice-related feedbacks in response to AER than to GHG forcing are found to be the crucial mechanism explaining this stronger AA. Our findings confirm the asymmetric Arctic climate response to AER and GHG forcing agents, which was recently reported in studies with models forced with increased and decreased CO<sub>2</sub> concentrations<sup>44,45</sup>.

An important implication to emerge from our findings is that the observed strengthening of AA over the past few decades<sup>3,4</sup> may have been aggravated by AER emissions reductions, mostly in Europe and North America<sup>15,16</sup>. Our results, therefore, highlight the importance of air quality regulations and clean air policies, such as the U.S. Clean Air Act<sup>46</sup>, in amplifying Arctic warming. As more widespread AER emissions reductions are likely to be implemented in the coming decades in most parts of the world, the need to mitigate GHG emissions becomes more urgent in order to avoid detrimental consequences on Arctic climate, ecosystems, and socioeconomics.

## Methods

### Observational datasets

In this study, we use three observational surface-air temperature (SAT) products: the Goddard Institute for Space Science of the National Aeronautics and Space Administration surface temperature analysis version 4 (GISTEMPv4)<sup>47,48</sup>, the Met Office Hadley Centre/Climatic Research Unit global surface temperature dataset version 5.0.1.0 (HadCRUT5)<sup>49</sup>, and the Berkeley Earth surface temperature dataset (BEST)<sup>50</sup>. These SAT datasets were compiled based on a combination of 2-meter temperature observations over the land and sea surface temperature (SST) over the ocean. We focus our analysis on the time spanning from 1920 to 2005 in line with the available time period of single forcing climate model simulations.

### Single forcing historical simulations

To investigate and quantify the global and Arctic responses to different forcing agents, we utilize the historical simulation products during the 1920–2005 period from the Detection and Attribution Model Intercomparison Project (DAMIP)<sup>22</sup> within the Sixth Phase of the Coupled Model Intercomparison Project (CMIP6)<sup>23</sup>. The first set of experiments considered in this study is the all forcing simulations, in which the participating models were forced with all forcing agents, including GHG, AER, ozone, land-use changes, and natural forcings (i.e., volcanic and solar irradiance). The second set is the GHG-only simulations, in which the models were forced solely with the time-varying GHG concentrations (i.e., carbon dioxide, methane, nitrous oxide, and chlorofluorocarbons) with other forcings fixed at their pre-industrial levels. The third set of simulations was

forced by only the time-varying anthropogenic AER forcings, with all other forcings held fixed at pre-industrial levels. It is noted that the AER forcings here include direct (scattering and absorbing) and indirect (aerosol-cloud interactions) effects, which combined influence the climate variability, such as the changes in temperature and surface energy budget<sup>51–53</sup>, and that the AER were predominantly emitted from Europe and North America before the mid-20th century<sup>26,27</sup>, peaking around the 1980s, and declining afterwards<sup>15</sup>. The epicenter of AER emissions has then shifted to southern and eastern Asia and their amounts are expected to decline in the future<sup>54,55</sup>. We refer the second and third sets of experiments above to as the “only-one” forcing simulations to signify that these simulations are driven solely by one forcing agent. To account for the effect of internal variability, we select only the models containing at least ten ensemble members. These models are CNRM-CM6-1 (10 members), CanESM5 (30 members), IPSL-CM6A-LR (10 members), and MIROC6 (10 members).

We also use the historical simulations from the single forcing large ensemble project of the Community Earth System Model version 1 (CESM1)<sup>24,56</sup>, which consists of the Community Atmosphere Model version 5 (CAM5), Parallel Ocean Program version 2 (POP2), Community Land Model version 4 (CLM4), and Los Alamos Sea Ice Model (CICE). In these simulations, the forcings were prescribed in an alternate way in that the single forcing of interest was fixed at its 1920 level but other forcings were allowed to vary with time. The data repository of this CESM1 single forcing project contains all forcing simulations (referred to as ALL) with 40 members, fixed AER forcing simulations (referred to as xAER) with 20 members, and fixed GHG forcing simulations (referred to as xGHG) with 20 members. Following Deser et al., the combined effects of internal variability and the response to AER or GHG forcing can be quantified as:

$$X_i|_{AER} = X_i|_{xAER} - 2\overline{X}|_{xAER} + \overline{X}|_{ALL} \quad (1)$$

$$X_i|_{GHG} = X_i|_{xGHG} - 2\overline{X}|_{xGHG} + \overline{X}|_{ALL} \quad (2)$$

where “X” represents the target variable (e.g., SAT), the subscript “i” represents an individual ensemble member, and an overbar represents the ensemble mean. We refer to this type of experiment as an “all-but-one” forcing experiment, and to this particular set of experiments using CESM1 as CESM1-fix1920.

We further conducted two additional sets of CESM1 simulations (using the large-ensemble configuration of the model) which are denoted as CESM1-fix1955. These are similar to CESM1-fix1920, but either the AER forcing (20 ensemble members) or the CO<sub>2</sub> forcing (10 ensemble members) is fixed at 1955 levels with all other forcings varying with time. We also use the fixed AER and CO<sub>2</sub> simulations (20 members each) from the Canadian Earth System Model version 5 (CanESM5)<sup>12,25</sup> and denote this simulation set as CanESM5-fix1955. To isolate the response to AER or CO<sub>2</sub> forcing in CESM1-fix1955 and CanESM5-fix1955, we calculate the ensemble-mean difference between the ALL experiment and the xAER or xCO<sub>2</sub> experiment. Note that all simulations in DAMIP and CanESM5-fix1955 are using CMIP6 forcings while CESM1-fix1920 and CESM1-fix1955 are using CMIP5 forcings, and that for simplicity, we often use “GHG” to refer to the response to both all GHG (DAMIP and CESM1-fix1920) or solely CO<sub>2</sub> (CESM1-fix1955 and CanESM5-fix1955).

We quantify the effective radiative forcing (ERF) from AER and GHG forcings using fixed sea surface temperature (SST) simulations from the Radiative Forcing Model Intercomparison Project (RFMIP)<sup>57</sup> within CMIP6. In these fixed SST simulations, forcings are allowed to vary with time during the period of 1850–2014, while the SSTs and sea-ice concentrations are fixed at their climatology values derived from pre-industrial simulations. We employ simulations that include either time-varying AER or GHG forcing, with all other forcings fixed at pre-industrial levels. These AER and GHG fixed SST simulations are available for the four DAMIP models used in this study. We compute the ERF as the difference between the net top-of-atmosphere (TOA) radiation in

these simulations and a control simulation with constant pre-industrial forcings.

### Arctic amplification factor

In this study, we define the Arctic region as 70°N–90°N and the global region as 90°N–90°S. We define the response ( $\Delta$ ) of a given target variable (e.g., surface air temperature, sea-ice area, albedo, and surface heat fluxes) to AER or GHG/CO<sub>2</sub> forcing as the 30-year linear trend of that variable between 1955 and 1984. To quantify the Arctic amplification, we calculate the Arctic amplification factor (AAF) as:

$$\overline{AAF|_j} = \frac{\overline{\Delta T_{Arctic}|_j}}{\overline{\Delta T_{Global}|_j}} \quad (3)$$

where  $\Delta T_{Arctic}$  represents the Arctic-averaged SAT response,  $\Delta T_{Global}$  denotes the globally-averaged SAT response, “ $|_j$ ” signifies the forcing agent (AER or GHG/CO<sub>2</sub>), and an overbar indicates the ensemble mean.

### Bootstrapping technique

To robustly assess the internal variability of the AAF within each model, we adopt a bootstrapping method<sup>58</sup>, which has been widely applied in climate change studies<sup>59–61</sup>. Specifically, we randomly sample ensemble members without replacement a total of 10,000 times, and then compute the average over resampled members to obtain 10,000 ensemble means. The resampled AAF can, thus, be expressed as:

$$(AAF|_j)_{resampled} = \frac{(\Delta T_{Arctic}|_j)_{resampled}}{(\Delta T_{Global}|_j)_{resampled}}, \quad (4)$$

where  $(\Delta T_{Arctic}|_j)_{resampled}$  and  $(\Delta T_{Global}|_j)_{resampled}$  are calculated using the same resampled members.

### Data availability

The GISTEMP data are available at <https://data.giss.nasa.gov/gistemp>, the HadCRUT5 data can be found at <https://www.metoffice.gov.uk/hadobs/hadcrut5>, and the BEST data can be obtained at <https://berkeleyearth.org/data>. DAMIP data can be downloaded at <https://esgf-node.llnl.gov/projects/cmip6>. CESM1-fix1920 can be found at <http://www.cesm.ucar.edu/experiments/cesm1.1/LE/#single-forcing>. CESM1-fix1955 and CanESM5-fix1955 can be downloaded from a Zenodo repository respectively (<https://zenodo.org/record/7469290> and <https://zenodo.org/records/6908225>).

### Code availability

The Python scripts for processing data and plotting figures are available on Y.-T. Wu’s Zenodo repository <https://zenodo.org/records/10628819>.

Received: 27 February 2024; Accepted: 12 June 2024;

Published online: 20 June 2024

### References

- Gulev, S. K. et al. Changing state of the climate system. In *Climate Change 2021: The Physical Science Basis. Contribution of Working Group I to the Sixth Assessment Report of the Intergovernmental Panel on Climate Change* (eds Masson-Delmotte, V. et al.) 287–422 (IPCC, 2021).
- Cohen, J. et al. Recent arctic amplification and extreme mid-latitude weather. *Nat. Geosci.* **7**, 627–637 (2014).
- Chylek, P. et al. Annual mean arctic amplification 1970–2020: observed and simulated by cmip6 climate models. *Geophys. Res. Lett.* **49**, e2022GL099371 (2022).
- Rantanen, M. et al. The arctic has warmed nearly four times faster than the globe since 1979. *Commun. Earth Environ.* **3**, 168 (2022).
- Cai, Z. et al. Arctic warming revealed by multiple cmip6 models: evaluation of historical simulations and quantification of future projection uncertainties. *J. Clim.* **34**, 4871–4892 (2021).
- Holland, M. M. & Landrum, L. The emergence and transient nature of arctic amplification in coupled climate models. *Front. Earth Sci.* **9**, 719024 (2021).
- Taylor, P. C. et al. Process drivers, inter-model spread, and the path forward: A review of amplified arctic warming. *Front. Earth Sci.* **9**, 758361 (2022).
- Wu, Y.-T. et al. Exploiting smiles and the cmip5 archive to understand arctic climate change seasonality and uncertainty. *Geophys. Res. Lett.* **50**, e2022GL100745 (2023).
- Manabe, S. & Wetherald, R. T. The effects of doubling the co 2 concentration on the climate of a general circulation model. *J. Atmos. Sci.* **32**, 3–15 (1975).
- Pithan, F. & Mauritsen, T. Arctic amplification dominated by temperature feedbacks in contemporary climate models. *Nat. Geosci.* **7**, 181–184 (2014).
- Polvani, L. M., Previdi, M., England, M. R., Chiodo, G. & Smith, K. L. Substantial twentieth-century arctic warming caused by ozone-depleting substances. *Nat. Clim. Change* **10**, 130–133 (2020).
- Sigmond, M. et al. Large contribution of ozone-depleting substances to global and arctic warming in the late 20th century. *Geophys. Res. Lett.* **50**, e2022GL100563 (2023).
- Najafi, M. R., Zwiers, F. W. & Gillett, N. P. Attribution of arctic temperature change to greenhouse-gas and aerosol influences. *Nat. Clim. Change* **5**, 246–249 (2015).
- England, M. R., Eisenman, I., Lutsko, N. J. & Wagner, T. J. The recent emergence of arctic amplification. *Geophys. Res. Lett.* **48**, e2021GL094086 (2021).
- Acosta Navarro, J. C. et al. Amplification of arctic warming by past air pollution reductions in europe. *Nat. Geosci.* **9**, 277–281 (2016).
- Shindell, D. & Faluvegi, G. Climate response to regional radiative forcing during the twentieth century. *Nat. Geosci.* **2**, 294–300 (2009).
- Stjern, C. W. et al. Arctic amplification response to individual climate drivers. *J. Geophys. Res. Atmospheres* **124**, 6698–6717 (2019).
- Deng, J., Dai, A. & Xu, H. Nonlinear climate responses to increasing co2 and anthropogenic aerosols simulated by cesm1. *J. Clim.* **33**, 281–301 (2020).
- Jiang, Y. et al. Impacts of wildfire aerosols on global energy budget and climate: The role of climate feedbacks. *J. Clim.* **33**, 3351–3366 (2020).
- Fan, X., Duan, Q., Shen, C., Wu, Y. & Xing, C. Global surface air temperatures in cmip6: historical performance and future changes. *Environ. Res. Lett.* **15**, 104056 (2020).
- England, M. R. Are multi-decadal fluctuations in arctic and antarctic surface temperatures a forced response to anthropogenic emissions or part of internal climate variability? *Geophys. Res. Lett.* **48**, e2020GL090631 (2021).
- Gillett, N. P. et al. The detection and attribution model intercomparison project (damip v1. 0) contribution to cmip6. *Geosci. Model Dev.* **9**, 3685–3697 (2016).
- Eyring, V. et al. Overview of the coupled model intercomparison project phase 6 (cmip6) experimental design and organization. *Geosci. Model Dev.* **9**, 1937–1958 (2016).
- Deser, C. et al. Isolating the evolving contributions of anthropogenic aerosols and greenhouse gases: a new cesm1 large ensemble community resource. *J. Clim.* **33**, 7835–7858 (2020).
- Swart, N. C. et al. The canadian earth system model version 5 (canesm5. 0.3). *Geosci. Model Dev.* **12**, 4823–4873 (2019).
- Lamarque, J.-F. et al. Historical (1850–2000) gridded anthropogenic and biomass burning emissions of reactive gases and aerosols: methodology and application. *Atmos. Chem. Phys.* **10**, 7017–7039 (2010).

27. Persad, G. G. & Caldeira, K. Divergent global-scale temperature effects from identical aerosols emitted in different regions. *Nat. Commun.* **9**, 3289 (2018).
28. Deser, C. et al. Insights from earth system model initial-condition large ensembles and future prospects. *Nat. Clim. Change* **10**, 277–286 (2020).
29. Lehner, F. et al. Partitioning climate projection uncertainty with multiple large ensembles and cmip5/6. *Earth Syst. Dyn.* **11**, 491–508 (2020).
30. Simpson, I. R. et al. The cesm2 single forcing large ensemble and comparison to cesm1: Implications for experimental design. *J. Clim.* **36**, 5687–5711 (2023).
31. Screen, J. A., Deser, C., Simmonds, I. & Tomas, R. Atmospheric impacts of arctic sea-ice loss, 1979–2009: Separating forced change from atmospheric internal variability. *Clim. Dyn.* **43**, 333–344 (2014).
32. Ding, Q. et al. Influence of high-latitude atmospheric circulation changes on summertime arctic sea ice. *Nat. Clim. Change* **7**, 289–295 (2017).
33. Dai, A., Luo, D., Song, M. & Liu, J. Arctic amplification is caused by sea-ice loss under increasing co<sub>2</sub>. *Nat. Commun.* **10**, 121 (2019).
34. Manabe, S. & Stouffer, R. J. Sensitivity of a global climate model to an increase of co<sub>2</sub> concentration in the atmosphere. *J. Geophys. Res. Oceans* **85**, 5529–5554 (1980).
35. Deser, C., Tomas, R., Alexander, M. & Lawrence, D. The seasonal atmospheric response to projected arctic sea ice loss in the late twenty-first century. *J. Clim.* **23**, 333–351 (2010).
36. Screen, J. A. & Simmonds, I. The central role of diminishing sea ice in recent arctic temperature amplification. *Nature* **464**, 1334–1337 (2010).
37. Chung, E.-S. et al. Cold-season arctic amplification driven by arctic ocean-mediated seasonal energy transfer. *Earths Fut.* **9**, e2020EF001898 (2021).
38. Hahn, L. C., Armour, K. C., Battisti, D. S., Eisenman, I. & Bitz, C. M. Seasonality in arctic warming driven by sea ice effective heat capacity. *J. Clim.* **35**, 1629–1642 (2022).
39. Liang, Y.-C., Polvani, L. M. & Mitevski, I. Arctic amplification, and its seasonal migration, over a wide range of abrupt co<sub>2</sub> forcing. *Npj Clim. Atmos. Sci.* **5**, 14 (2022).
40. Serreze, M., Barrett, A., Stroeve, J., Kindig, D. & Holland, M. The emergence of surface-based arctic amplification. *Cryosphere* **3**, 11–19 (2009).
41. Graverson, R. G., Langen, P. L. & Mauritsen, T. Polar amplification in ccsm4: Contributions from the lapse rate and surface albedo feedbacks. *J. Clim.* **27**, 4433–4450 (2014).
42. Lainé, A., Yoshimori, M. & Abe-Ouchi, A. Surface arctic amplification factors in cmip5 models: land and oceanic surfaces and seasonality. *J. Clim.* **29**, 3297–3316 (2016).
43. Boeke, R. C. & Taylor, P. C. Seasonal energy exchange in sea ice retreat regions contributes to differences in projected arctic warming. *Nat. Commun.* **9**, 5017 (2018).
44. Mitevski, I., Polvani, L. M. & Orbe, C. Asymmetric warming/cooling response to co<sub>2</sub> increase/decrease mainly due to non-logarithmic forcing, not feedbacks. *Geophys. Res. Lett.* **49**, e2021GL097133 (2022).
45. Zhou, S.-N., Liang, Y.-C., Mitevski, I. & Polvani, L. M. Stronger arctic amplification produced by decreasing, not increasing, co<sub>2</sub> concentrations. *Environ. Res. Clim.* **2**, 045001 (2023).
46. Clean Air Act Amendments of 1990, P.L. 101–549, 104 Stat. 2399 (1990).
47. NASA. Giss surface temperature analysis (GISTEMP), 23. NASA Goddard Institute for Space Studies. Accessed on the internet at <https://data.giss.nasa.gov/gistemp> (2023).
48. Lenssen, N. J. et al. Improvements in the gistemp uncertainty model. *J. Geophys. Res. Atmos.* **124**, 6307–6326 (2019).
49. Morice, C. P. et al. An updated assessment of near-surface temperature change from 1850: the hadcrut5 data set. *J. Geophys. Res. Atmos.* **126**, e2019JD032361 (2021).
50. Rohde, R. A. & Hausfather, Z. The berkeley earth land/ocean temperature record. *Earth Syst. Sci. Data* **12**, 3469–3479 (2020).
51. Middlemas, E., Kay, J., Medeiros, B. & Maroon, E. Quantifying the influence of cloud radiative feedbacks on arctic surface warming using cloud locking in an earth system model. *Geophys. Res. Lett.* **47**, e2020GL089207 (2020).
52. Danabasoglu, G. et al. The community earth system model version 2 (cesm2). *J. Adv. Model. Earth Syst.* **12**, e2019MS001916 (2020).
53. Chalmers, J., Kay, J. E., Middlemas, E. A., Maroon, E. A. & DiNezio, P. Does disabling cloud radiative feedbacks change spatial patterns of surface greenhouse warming and cooling? *J. Clim.* **35**, 1787–1807 (2022).
54. Samset, B. H., Lund, M. T., Bollasina, M., Myhre, G. & Wilcox, L. Emerging asian aerosol patterns. *Nat. Geosci.* **12**, 582–584 (2019).
55. Xiang, B., Xie, S.-P., Kang, S. M. & Kramer, R. J. An emerging asian aerosol dipole pattern reshapes the asian summer monsoon and exacerbates northern hemisphere warming. *npj Clim. Atmos. Sci.* **6**, 77 (2023).
56. Kay, J. E. et al. The community earth system model (cesm) large ensemble project: A community resource for studying climate change in the presence of internal climate variability. *Bull. Am. Meteorological Soc.* **96**, 1333–1349 (2015).
57. Smith, C. J. et al. Effective radiative forcing and adjustments in cmip6 models. *Atmos. Chem. Phys.* **20**, 9591–9618 (2020).
58. Pedregosa, F. et al. Scikit-learn: Machine learning in python. *J. Mach. Learn. Res.* **12**, 2825–2830 (2011).
59. Liang, Y.-C. et al. Stronger arctic amplification from ozone-depleting substances than from carbon dioxide. *Environ. Res. Lett.* **17**, 024010 (2022).
60. Oehrlein, J., Polvani, L. M., Sun, L. & Deser, C. How well do we know the surface impact of sudden stratospheric warmings? *Geophys. Res. Lett.* **48**, e2021GL095493 (2021).
61. Sun, L., Deser, C., Simpson, I. & Sigmond, M. Uncertainty in the winter tropospheric response to arctic sea ice loss: The role of stratospheric polar vortex internal variability. *J. Clim.* **35**, 3109–3130 (2022).

## Acknowledgements

Y.-T.W. and Y.-C.L. are supported by grants from the National Science and Technology Council (110-2111-M-002-019-MY2, 111-2628-M-002-011, and 112-2628-M-002-009) to National Taiwan University. L.M.P. and M.P. are supported by a grant from the U.S. National Science Foundation to Columbia University. M.R.E. is supported by a Royal Commission for the Exhibition of 1851 research fellowship. We thank Dr Clara Deser at NCAR and Dr Yen-Ting Hwang at National Taiwan University for their constructive comments and suggestions to improve the quality of this manuscript. We thank to National Center for High-performance Computing (NCHC) of National Applied Research Laboratories (NARLabs) in Taiwan for providing computational and storage resources.

## Author contributions

Y.-T. Wu, Y.-C. Liang, M. Previdi, and L. M. Polvani conceived the study. Y.-T. Wu performed the analyses and Y.-C. Liang conducted the CESM1-fix1955 AER simulations. M.R. England conducted the CESM1-fix1955 CO<sub>2</sub> simulations. M. Sigmond provides the simulations from the CanESM5. Y.-T. Wu and Y.-C. Liang prepared the initial manuscript draft and all authors contributed to the manuscript writing. All authors contributed to the interpretation of the results.

### Competing interests

The authors declare no competing interests.

### Additional information

**Supplementary information** The online version contains supplementary material available at

<https://doi.org/10.1038/s41612-024-00696-0>.

**Correspondence** and requests for materials should be addressed to Yu-Chiao Liang.

**Reprints and permissions information** is available at <http://www.nature.com/reprints>

**Publisher's note** Springer Nature remains neutral with regard to jurisdictional claims in published maps and institutional affiliations.

**Open Access** This article is licensed under a Creative Commons Attribution 4.0 International License, which permits use, sharing, adaptation, distribution and reproduction in any medium or format, as long as you give appropriate credit to the original author(s) and the source, provide a link to the Creative Commons licence, and indicate if changes were made. The images or other third party material in this article are included in the article's Creative Commons licence, unless indicated otherwise in a credit line to the material. If material is not included in the article's Creative Commons licence and your intended use is not permitted by statutory regulation or exceeds the permitted use, you will need to obtain permission directly from the copyright holder. To view a copy of this licence, visit <http://creativecommons.org/licenses/by/4.0/>.

© The Author(s) 2024